Available online at www.sciencedirect.com
ScienceDirect
Journal of the European Ceramic Society 29 (2009) 2235–2248
www.elsevier.com/locate/jeurceramsoc

# Onset coarsening-coalescence kinetics of γ-type related $Al_2O_3$ nanoparticles: Implications to their assembly in a laser ablation process

I-Lung Liu, Pouyan Shen *

*Institute of Materials Science and Engineering, Department of Materials and Optoelectronic Science, National Sun Yat-sen University, Kaohsiung 80424, Taiwan, ROC*

Received 19 September 2008; received in revised form 3 November 2008; accepted 15 November 2008
Available online 12 February 2009

**Abstract**

An onset coarsening-coalescence event based on the incubation time of cylindrical mesopore formation and a significant decrease of specific surface area by 50% and 70% relative to the dry pressed samples was determined by $N_2$ adsorption–desorption hysteresis isotherm for two $Al_2O_3$ powders having 50 and 10 nm in diameter respectively on an average and with γ-type related structures, i.e. γ- and its distortion derivatives δ- and/or θ-types with {1 0 0}/{1 1 1} facets and twinning according to transmission electron microscopy. In the temperature range of 1100–1400 °C, both powders underwent onset coarsening-coalescence before reconstructive transformation to form the stable α-type. The apparent activation energy for such a rapid coarsening-coalescence event was estimated as 241 ± 18 and 119 ± 19 kJ/mol, for 50 and 10 nm-sized particles, respectively indicating easier surface diffusion and particle movement for the latter. The size dependence of surface relaxation and onset coarsening-coalescence of the γ-type related $Al_2O_3$ nanoparticles agrees with their recrystallization–repacking upon electron irradiation and accounts for their assembly into nano chain aggregates or a close packed manner under the radiant heating effect in a dynamic laser ablation process.


*Keywords:* Coarsening-coalescence; γ-$Al_2O_3$; BET; TEM

## 1. Introduction

$Al_2O_3$ exists as the thermodynamically stable α-type, i.e. corundum with hexagonal close packing of oxygen, and a number of metastable polymorphs with face-centered close (fcc) packing of oxygen, i.e. γ-type in cubic spinel type structure and its distortion derivatives such as δ-form in tetragonal or orthorhombic structure and θ-form in monoclinic structure.[1] The motivation of this research is to determine a vigorous onset coarsening-coalescence event for the γ-type related $Al_2O_3$ nanoparticles before their transformation into the stable α-type structure. This subject is of concern to the phase behavior of the metastable $Al_2O_3$ nanocondensates produced in a laser ablation process.

Micron size α-$Al_2O_3$ powders sintering toward 100% theoretical density for a wide engineering application have been extensively studied at relatively high temperatures, typically near or above 1600 °C, where the α-type $Al_2O_3$ is stable. For example, it took more than an hour to reach 95% relative density with considerable abnormal grain growth at 1630 °C for α-$Al_2O_3$ powders 99.99% in purity.[2] This is however not representative of the current state of the art using much finer sized particles. It is a general belief that melting point decreases considerably with size reduction under the influence of capillarity effect as proved by in situ transmission electron microscopic observations of semiconductor nanocrystals.[3] Having a lower melting point, finer sized α-$Al_2O_3$ particles are expected to have fair sinterability at relatively low temperatures because of a relatively high homologous temperature ($T/T_m$, where $T_m$ is melting point). The size effect on sintering also arises from geometrical aspects of the Herring model, i.e. the mass transport rate is proportional to $1/G^n$ where $G$ is the particle or grain size and $n$ is an exponent related to the mass transport mechanism.[4] Indeed, submicron sized α-$Al_2O_3$ powders were shown to sinter in the temperature range 1150–1275 °C focusing on particle agglomeration and the evolution of pore structures during sintering,[5] and nanocrystalline α-$Al_2O_3$ powders prepared by a precipitation method were able to sinter from 1200

* Corresponding author.
*E-mail address:* pshen@mail.nsysu.edu.tw (P. Shen).

0955-2219/$ – see front matter © 2009 Elsevier Ltd. All rights reserved.
doi:10.1016/j.jeurceramsoc.2008.11.020

to 900 °C.[6] The initial stage sintering of such powders in soft and hard agglomeration was found to have activation energies of 365 and 492 kJ/mol, respectively both being controlled by grain boundary diffusion based on the observed relationship between the linear shrinkage strain of the compact and the residence time.[6] In addition, sintering temperature depression to approximately 1100–1200 °C for nanosized α-$Al_2O_3$ powders prepared by mechanical milling[7,8] was attributed to small size and dense packing of the crystallites rather than to lattice imperfections.[7]

Little attention was paid to the sintering of metastable γ-type $Al_2O_3$ which is favorable in the nanosize regime due to its lower surface energy yet higher entropy than α-$Al_2O_3$.[9,10] Pressureless sintering of the metastable precursors of α-$Al_2O_3$ generally requires rather high temperatures above ca. 1100 °C[11–14] due to large and extensive pore network developed during the transformation to α-$Al_2O_3$.[11] Sintering of acicular γ-$Al_2O_3$ derived from dehydrated pseudo-boehmite was shown by surface area measurements to involve a steep drop of the surface area due to the solid state reaction to α-$Al_2O_3$.[14] It was established that the rate-limiting step of the sintering is nucleation of α-$Al_2O_3$, and the contacts between the elementary alumina particles dominate the sinter process.[14] However, it is not clear if particle coarsening and/or coalescence are more important than sintering for compact γ-$Al_2O_3$ nanoparticles.

Recently, pulsed laser ablation on an Al target in air was shown to produce nanosize γ-$Al_2O_3$ condensates, nearly spherical yet with (*h k l*)-specific facets, which assembled as nano chain aggregate (NCA) and sinter/coalesce further into a close packed manner,[15] analogous to $TiO_2$ nanocondensates prepared by gas evaporation[16] or laser ablation.[17,18] It was suggested that radiant heating could be sufficient at least up to 1000 °C in a dynamic laser ablation process for effective sintering/coalescence of the γ-$Al_2O_3$ nanocondensates to occur despite their low surface energy.[15] Still, static heating experiments are required to clarify how quick the γ-$Al_2O_3$ nanoparticles can be thermally activated for vigorous coarsening-coalescence or sintering before their reconstruction into the stable α-type at high temperatures.

Here, isothermal onset coarsening-coalescence of γ-$Al_2O_3$-type related nanoparticles was studied in the temperature range of 1100–1400 °C. We focused on a rather short incubation time for the cylindrical mesopore formation with an accompanied significant change of specific surface area, as characteristic of onset coarsening-coalescence. Such a rapid onset coarsening-coalescence process was satisfactorily determined by $N_2$ adsorption–desorption hysteresis isotherm and auxiliary in situ observations of powders during electron irradiation. A vigorous onset coarsening-coalescence event for the γ-type related $Al_2O_3$ powders with a mean particle diameter of 10 and 50 nm respectively sheds light on size dependent surface state and hence surface diffusion-controlled coarsening-coalescence in a dynamic laser ablation process.

## 2. Experimental

$Al_2O_3$ powders (99.9%, Aldrich) with a mean particle diameter of 50 or 10 nm were die-pressed at 650 MPa into disks ca. 5 mm in diameter and 2 mm in thickness. The disks were fired in 10 min increments at 1100 and 1200 °C or alternatively in 2 min increments at 1300 and 1400 °C in air, until onset coarsening-coalescence was noted by the type of adsorption–desorption hysteresis isotherm. The starting powders were dispersed on a carbon-coated collodion film for phase, shape and size distribution characterizations using transmission electron microscopy (TEM, JEOL3010 at 300 kV). Microstructure changes of the samples due to dry pressing and heating were studied by scanning electron microscopy (SEM, JEOL 6330 at 20 kV). The phase identity of the dry pressed and heat treated samples was determined mainly by X-ray diffraction (XRD, CuKα, 40 kV, 30 mA at 0.05° and 3 s per step). In situ TEM (FEI Tecnai G2 F20 at 200 kV) observations were also conducted at a specified spot size 1.5 nm and beam current 5 nA to study the phase behavior of the individual $Al_2O_3$ particles under the influence of electron irradiation for up to 60 min.

Nitrogen adsorption/desorption isotherms of the dry pressed and then heated powders were conducted at liquid nitrogen temperature of 196 °C using a Micromeritics ASAP 2020 instrument. The surface area and pore size distributions were obtained from the $N_2$ adsorption and desorption branch, using the Brunauer–Emmett–Teller (BET) method[19] and Barrett–Joyner–Halenda (BJH) method,[20] in low and high relative pressure ($P/P_o$) range, respectively where $P_o$ is the saturation pressure determined as 760–762 mmHg. A filler rod containing ca. 0.1 g of $Al_2O_3$ sample with a theoretical density of 3.9–4.0 g/cm$^3$ (assuming a negligible difference from that of the α-type) was pumped down to $10^{-3}$ Torr for degassing at 300 °C followed by BET/BJH measurements at a relative pressure increment 0.05. The BET isotherm and BJH adsorption/desorption hysteresis type of the samples are classified according to the scheme of International Union of Pure and Applied Chemistry (IUPAC).[21] The H1 type adsorption/desorption hysteresis loop of the type IV isotherm (Fig. A.1) was used as an indicator of cylindrical pore formation and onset sintering.

## 3. Results

### 3.1. Shape of the starting powders

TEM bright field images (BFI) and corresponding selected area electron diffraction (SAED) patterns compiled in Fig. 1a indicated that the nearly spherical powders with an average diameter of 50 nm include the γ-type free of twinning together with its distortion derivatives, i.e. δ- and/or θ-types with {1 0 0}/{1 1 1} facets and twinning. As a comparison, the powders with an average diameter of 10 nm are predominantly γ-type with {1 0 0} facets (Fig. 2) in addition to {1 1 1} facets known to facilitate a {*h k l*}-specific coalescence process in the case of nanocondensates prepared via a dynamic laser ablation process.[15] It should be noted that minor δ-type also exists in the 10 nm-sized powders according to XRD with a much larger sampling volume.

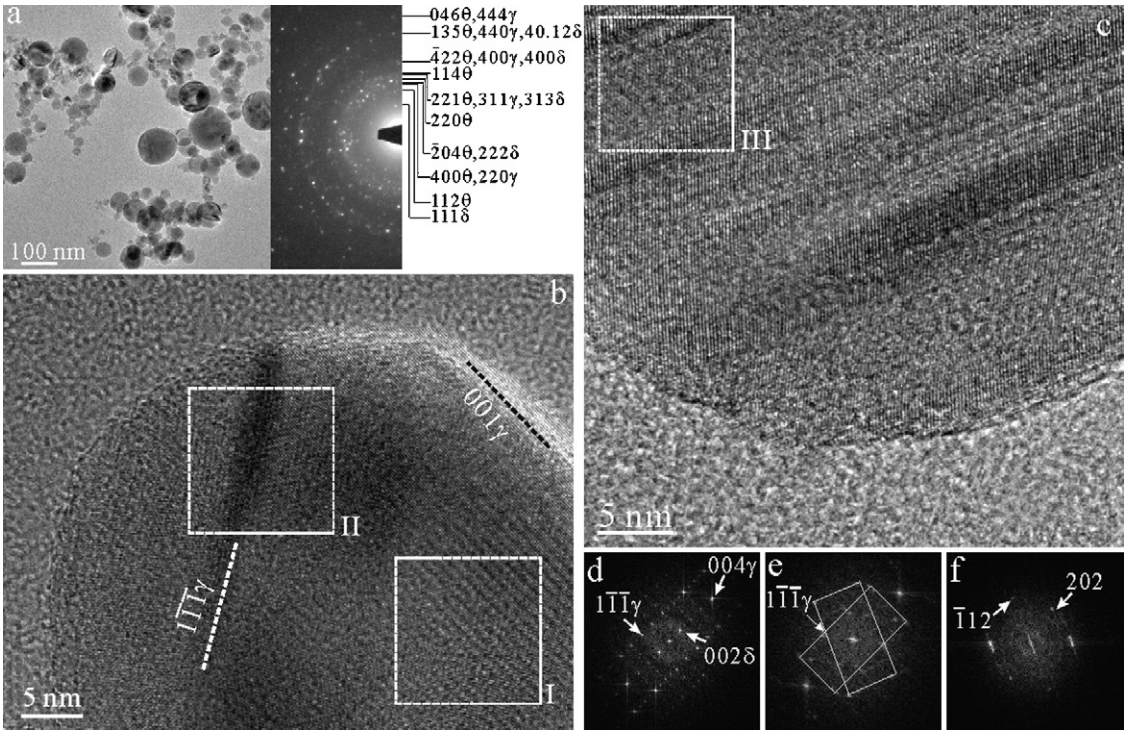


Fig. 1. (a) TEM bright field image and corresponding SAED pattern of $Al_2O_3$ particles having an average diameter of 50 nm and γ-type related structures as indicated by *h k l* of each phase labeled. (b) Lattice image of a typical δ + γ particle with (0 0 1) facet and (1 $\bar{1}$ $\bar{1}$) twin plane (denoted as dotted line) which is parallel to (1 $\bar{1}$ $\bar{1}$) facet to the left of the particle. The 2-D Fourier transforms (d) and (e) from square regions I and II show single crystal in [1 1 0] zone axis and reciprocal lattice units in twin relationship as outlined, respectively. (c) Lattice image of a representative θ-type particle with polysynthetic ($\bar{1}$ 1 2) faulting or twinning in [1 3 $\bar{1}$] zone axis according to 2-D Fourier transform (f) from region III.

### 3.2. Phase identity of the dry pressed powders upon heating

The typical XRD traces of the dry pressed and further heated powder batches of a mean particle diameter of 50 and 10 nm are shown in Figs. A.2 and A.3, respectively and the relative abundance of phases based on strong to moderate strong XRD peaks according to JCPDS files and ref. 22 are compiled in Tables 1 and 2 for the 50 and 10 nm-sized powders, respectively. Dry pressing caused a significant {1 1 1} preferred orientation of the γ + δ phases for 10 nm-sized but not 50 nm-sized powders (Figs. A.2a versus A.3a). Such a preferred orientation can be attributed to the well-developed {1 1 1} surfaces of the 10 nm-sized particles for (*h k l*)-specific packing during dry pressing.

Upon heating for a specific time period, both samples underwent phase change into θ- and then the stable α-type structure with a critical size of phase transformation.[23] For example, the 50 nm-sized powders changed into α-type with negligible θ-type relic when fired for 30 min at 1200 °C (Fig. A.2b), yet changed completely into the stable α-type when fired for the same time period at a higher temperature 1300 °C (Fig. A.2c). The γ-, δ- and θ-$Al_2O_3$ almost remained unchanged when fired shortly, e.g. 1 min at 1400 °C for such sized powder batch (Fig. A.2d).

As for the 10 nm-sized θ-$Al_2O_3$ powders, partial transformation into α-type occurred when fired at 1200 °C for 30 min (Fig. A.3b), or 1300 °C for 5 min (Fig. A.3c). The γ-, δ- and abundant θ-$Al_2O_3$ remained in such sized sample when fired at 1400 °C for 2 min (Fig. A.3d), indicating an incubation time is

Table 1
BET/BJH data and phase identity of 50 nm-sized $Al_2O_3$ powder subjected to various treatments.

| *T*(°C)-*t*(min) | Specific surface area ($m^2$/g) | Ads./desorp. pore width (nm) | Phases |
|---|---|---|---|
| Dry pressed | 35.35 | 21.0/16.7 | γ + δ > θ |
| 1100-10 | 26.21 | 21.1/16.1 | θ > γ + δ |
| 1100-20 | 25.12 | 22.9/16.4 | θ > γ + δ |
| 1100-30 | 25.30 | 23.4/16.9 | θ > γ + δ |
| 1100-40 | 26.29 | 22.0/16.4 | θ > γ + δ |
| 1100-50 | 23.00 | 23.6/16.7 | θ > γ + δ |
| 1100-60 | 25.83 | 22.5/16.4 | θ > γ + δ |
| 1100-70 | 18.80 | 28.4/19.0 | θ > γ + δ |
| 1100-80 | 22.54 | 26.3/17.4 | θ > γ + δ |
| 1100-90 | 11.63 | 28.8/23.0 | θ > γ + δ |
| 1200-10 | 17.38 | 24.7/17.7 | θ > γ + δ |
| 1200-20 | 7.03 | 42.7/34.2 | θ > γ + δ > α |
| 1200-30 | 5.40 | 40.6/29.6 | α |
| 1200-40 | 5.22 | 37.3/28.0 | α |
| 1200-50 | 4.65 | 29.7/25.5 | α |
| 1200-60 | 4.98 | 25.5/23.5 | α |
| 1300-2 | 29.09 | 21.3/16.7 | θ > γ + δ |
| 1300-4 | 7.85 | 40.8/26.0 | α > θ |
| 1300-6 | 6.72 | 41.8/31.1 | α |
| 1300-8 | 6.20 | 46.5/33.7 | α |
| 1400-1 | 31.20 | 20.7/16.2 | γ + δ > θ |
| 1400-3 | 11.46 | 33.2/21.5 | α > θ |
| 1400-5 | 6.84 | 25.3/22.9 | α |

*Note*: The abbreviation ads./desorp. denotes adsorption/desorption and the relative abundance of phases is based on XRD and TEM.

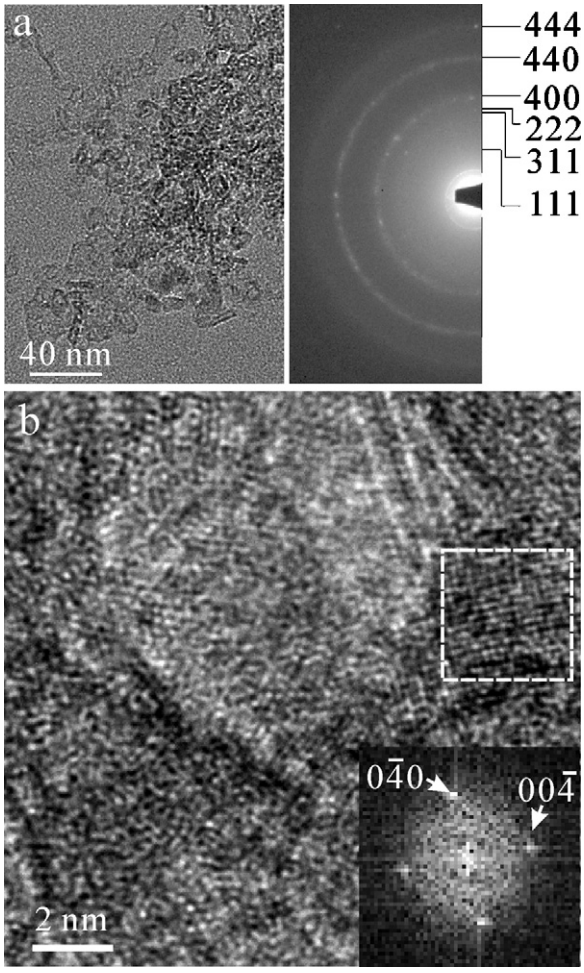


Fig. 2. (a) TEM bright field image and corresponding SAED pattern of $Al_2O_3$ particles having an average diameter of 10 nm and a predominant γ-type structure, as indicated by (*h k l*)s labeled. Electron irradiation has caused significant amorphization of the particles and hence diffuse diffraction to obscure (1 1 1) and its multiples of the γ-type structure. (b) Lattice image of an individual particle and 2-D forward transform (inset) of the square region showing (0 1 0) and (0 0 1) facets of the γ phase edge on in [1 0 0] zone axis.

required for the reconstructive θ → α transformation even at this high temperature.

### *3.3. Specific surface area, pore and microstructure changes upon heating*

BET data of the fired samples indicated that the specific surface area decreases whereas average pore size increases with the increase of dwelling time at a specific firing temperature for both 50 and 10 nm-sized $Al_2O_3$ powders as compiled in Tables 1 and 2, respectively. The drastic change of specific surface area and average pore size are related to the formation of cylindrical and/or truncated pores as further revealed by the following BJH analyses.

The BJH $N_2$ adsorption–desorption hysteresis isotherms for the 50 nm-sized $Al_2O_3$ powders dry pressed and further fired at 1100, 1200, 1300 and 1400 °C for specified time periods are shown in Fig. 3a–d, respectively. As shown in Fig. 3a, the hysteresis loop is H2 type (Fig. A.1) for the dry pressed sample but approaching H1 type for the samples heated at 1100 °C for 10–90 min. There is a significant decrease of the specific surface area by 50% with respect to the dry pressed sample at 80–90 min (Table 1, cf. rate curves in Fig. A.4), which corresponds to a steady coarsening-coalescence process as discussed later. In general, the hysteresis loops are in the relative pressure range 0.8 and 1.0 (i.e. actual pressure range 608–762 mmHg) for these samples. The time to form such a H1 type loop decreases with the increase of firing temperature, i.e. $10 \pm 5$, $3 \pm 1$, and $2 \pm 1$ min, accompanied with a significant decrease of specific surface area with respect to the dry pressed sample by ∼50% at 1200, 1300 and 1400 °C, respectively (Fig. 3b–d). A longer firing time in this temperature range caused the change of H1 type loop into irregular shape, presumably due to the formation of the truncated pores from cylindrical ones. In general, such a deteriorating loop shifts toward a higher relative pressure 0.9–1.0, i.e. actual pressure range 690–760 mmHg as indicated by the samples fired beyond 20 min at 1200 °C (Fig. 3b), beyond 4 min at 1300 °C and 1400 °C (Fig. 3c and d, respectively).

The adsorption–desorption hysteresis isotherms are quite different for the samples made of 10 nm-sized $Al_2O_3$ powders as compiled in Fig. 4. The green body consisting of such sized powders shows a H4 type loop in the relative pressure range 0.4–1.0, which is characteristic of narrow slit-like pores.[21] This indicates a nanosize effect on the surface state of the γ-type related $Al_2O_3$ powders as discussed later. The loop shifts to a higher relative pressure and changes into H1 type corresponding to cylindrical pores for the samples fired for ca. 10 min at

Table 2
BET/BJH data and phase identity of 10 nm-sized $Al_2O_3$ powder subjected to various treatments.

| *T*(°C)-*t*(min) | Specific surface area ($m^2$/g) | Ads./desorp. pore width (nm) | Phases |
|---|---|---|---|
| Dry pressed | 268.91 | 6.2/5.4 | γ > δ > θ |
| 1100-10 | 89.42 | 14.3/11.5 | θ > γ + δ |
| 1100-15 | 83.07 | 11.8/9.3 | θ > γ + δ |
| 1100-20 | 68.35 | 13.6/11.1 | θ > γ + δ |
| 1100-30 | 63.51 | 13.5/11.3 | θ > γ + δ |
| 1100-40 | 59.16 | 15.5/12.4 | θ > γ + δ |
| 1100-50 | 52.59 | 17.2/13.8 | θ > γ + δ |
| 1100-60 | 53.71 | 17.8/14.8 | θ > γ + δ |
| 1200-5 | 86.23 | 11.4/9.1 | θ > γ + δ |
| 1200-10 | 76.04 | 12.3/10.1 | θ > γ + δ |
| 1200-20 | 49.79 | 16.6/13.2 | α > θ > γ + δ |
| 1200-30 | 39.00 | 20.7/18.0 | α > θ |
| 1200-40 | 40.23 | 18.6/16.0 | α > θ |
| 1200-50 | 24.25 | 26.4/23.4 | α |
| 1200-60 | 18.20 | 29.8/26.8 | α |
| 1300-3 | 81.71 | 11.3/8.8 | θ > γ + δ |
| 1300-5 | 69.41 | 13.1/10.5 | θ > γ + δ > α |
| 1300-10 | 18.83 | 34.7/27.7 | α |
| 1300-20 | 8.57 | 21.4/19.6 | α |
| 1400-2 | 91.53 | 10.4/8.4 | θ > γ + δ |
| 1400-3 | 51.91 | 15.7/12.2 | θ > γ + δ |
| 1400-5 | 9.28 | 51.9/35.0 | α |

*Note*: The abbreviation ads./desorp. denotes adsorption/desorption and the relative abundance of phases is based on XRD and TEM.

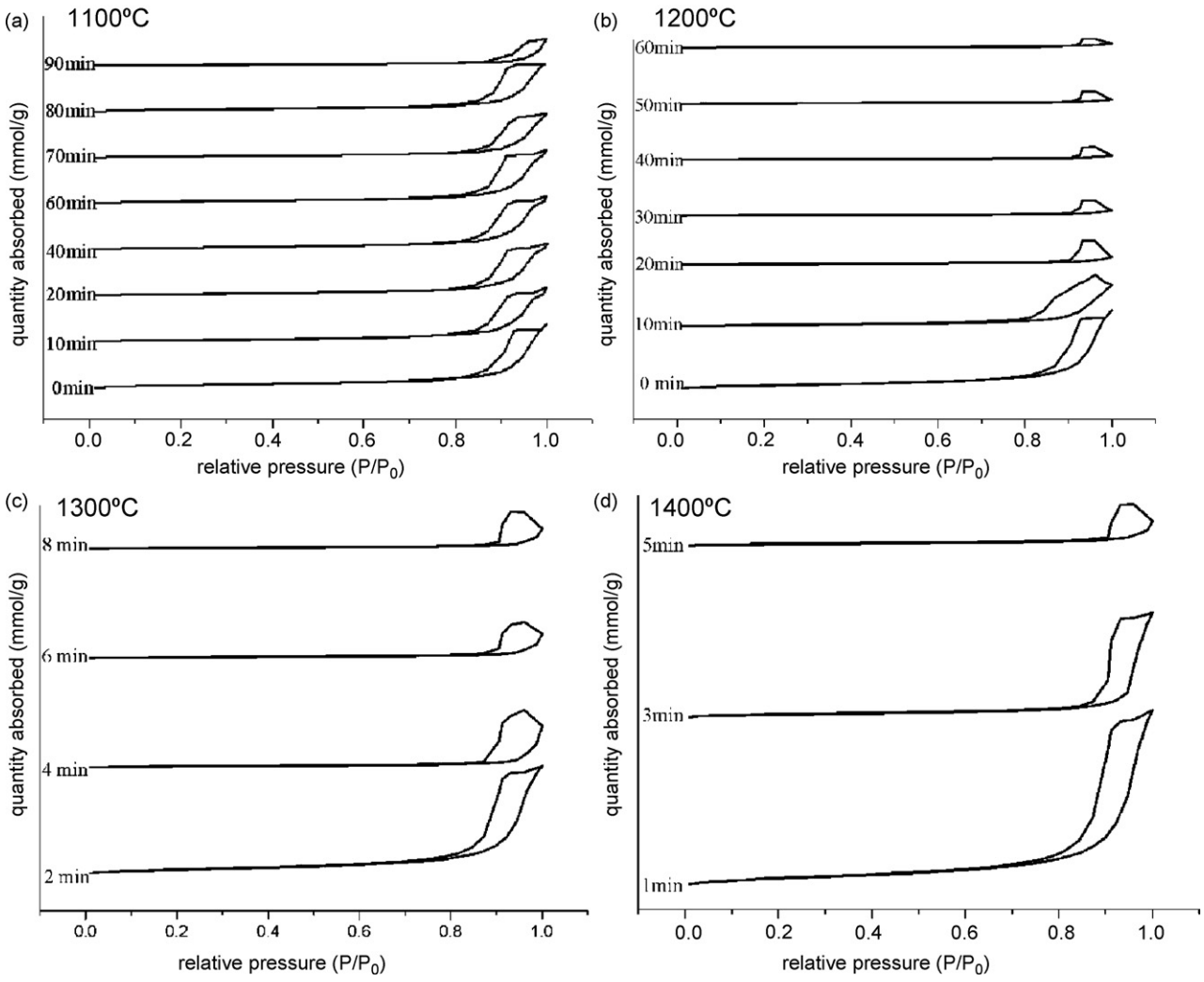


Fig. 3. BJH $N_2$ adsorption–desorption hysteresis isotherms of the $Al_2O_3$ powder with an average size of 50 nm and subjected to the specified heating treatments: (a) 1100 °C, 0–90 min, (b) 1200 °C, 0–60 min, (c) 1300 °C, 2–8 min, (d) 1400 °C, 1–5 min.

1100 °C (Fig. 4a), ca. 5 min at 1200 °C (Fig. 4b), ca. 3 min at 1300 °C (Fig. 4c) and ca. 2 min at 1400 °C (Fig. 4d). Considering further a more drastic decrease (70%) of the specific surface area relative to the dry pressed sample (Table 2, cf. rate curves in Fig. A.5) than the case of 50 nm-sized samples (Table 1, cf. rate curves in Fig. A.4), the onset time $t_{0.7}$, i.e. for a total of 70% drop of the specific surface area and accompanied cylindrical pore formation, in the 10 nm-sized samples was determined as $12 \pm 2$, $7 \pm 1$, $3 \pm 0.5$ and $2 \pm 0.2$ min for 1100, 1200, 1300 and 1400 °C, respectively. The H1 type loops are less well defined for the 10 nm-sized samples (Fig. 4) than the case of 50 nm-sized samples (Fig. 3). This indicates that the cylindrical pores at the triple junctions of the finer sized nanoparticles are smaller in aspect ratio. A longer firing time in this temperature range improves the H1 type loop, presumably due to repacking of the nano-sized powders as discussed later, and shifts it toward a higher relative pressure 0.9–1.0, as indicated by the samples fired beyond 60 min at 1200 °C (Fig. 4b), 10 min at 1300 °C (Fig. 4c) and 5 min at 1400 °C (Fig. 4d).

### *3.4. SEM observations of dry pressed and further heated samples*

In general, dry pressing did not cause appreciable cracking and particle size change but cause significant agglomeration for the finer sized particles as indicated by SEM secondary electron images of the two samples with different average particle size in Figs. 5a and 6a. In fact, the dry pressed powder with an average diameter of 50 nm showed varied size of pores among the particles with a wide size distribution (Fig. 5a). By contrast, the sample dry pressed with an average particle diameter of 10 nm has relatively uniform pore size at grain corners (Fig. 6a). In both cases, the cylindrical pores characteristic of slightly sintered bodies are vague, and the relative density is difficult, if not impossible, to measure because the dry pressed powders tended to disperse in water during such measurements.

The presence of cylindrical and truncated pores, an indicator of onset and further coarsening/coalescence or even sintering, in the samples fired for a suitable time period at a specified temperature was confirmed by SEM observations, as shown

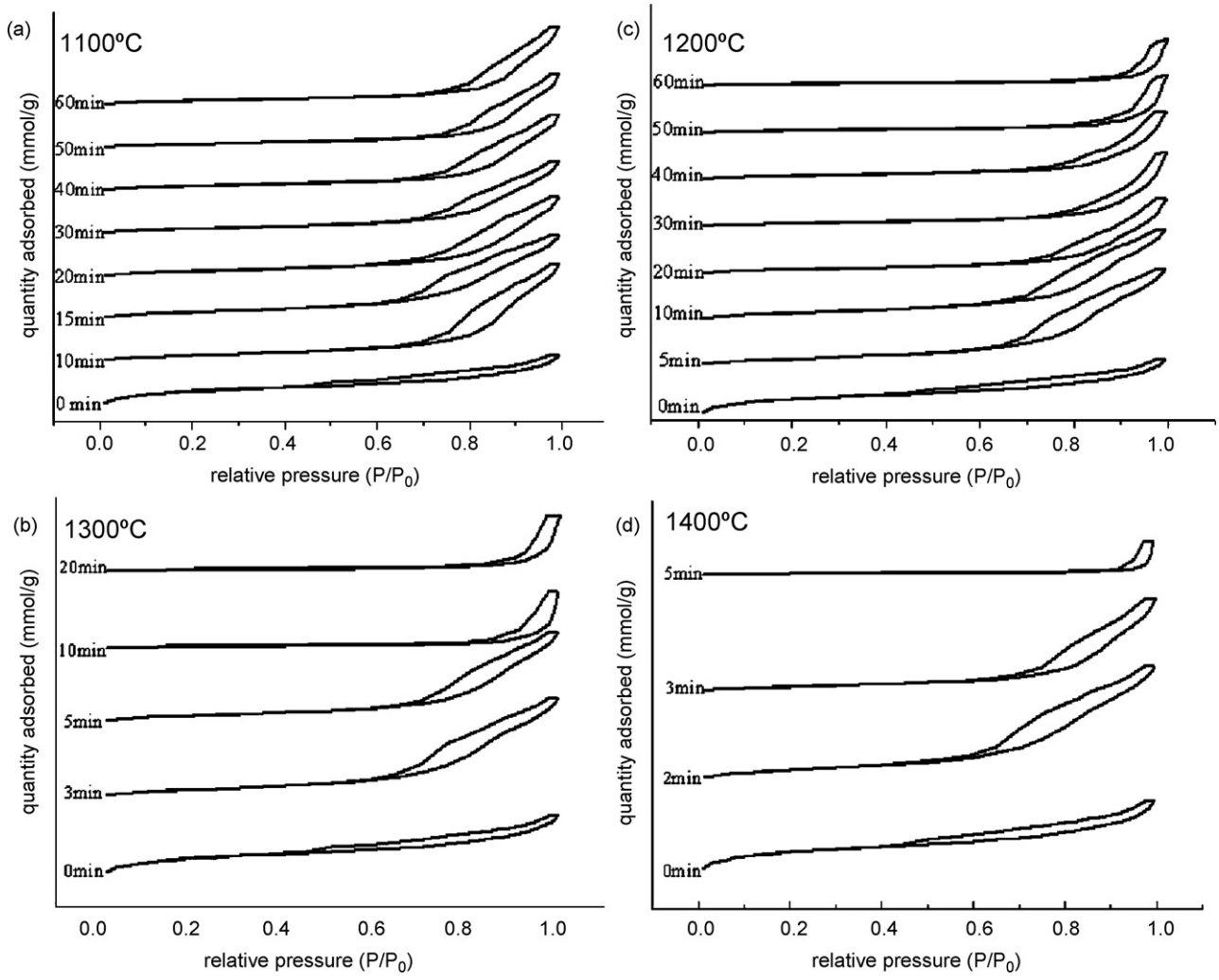


Fig. 4. BJH $N_2$ adsorption–desorption hysteresis isotherms of the $Al_2O_3$ powder with an average size of 10 nm and subjected to the specified heating treatments: (a) 1100 °C, 0–60 min, (b) 1200 °C, 0–60 min, (c) 1300 °C, 0–20 min, (d) 1400 °C, 0–5 min.

in Figs. 5 and 6, for the case of 50 and 10 nm-sized powders, respectively. Significant repacking and coalescence of slightly coarsened particles was observed to be associated with the sintering process in particular for the finer particles as numbered in a magnified image in Fig. 6c.

### *3.5. Phase behavior of the particles under electron beam heating*

For a better understanding of the phase behavior, in particular the coarsening, repacking and coalescence of the particles, in situ TEM observations of the powders in agglomeration were conducted under a specified beam size and beam current, as mentioned, for a considerable heating effect. The $Al_2O_3$ particles with an average size of 50 nm typically suffered surface amorphization followed by cellular/dendritic crystallization to form new γ-$Al_2O_3$ droplets ca. 5 nm in diameter when electron irradiated for 30 min (Fig. 7a). After electron irradiation for 60 min, a combined coarsening, repacking and coalescence process typically occurred for the newly formed γ-$Al_2O_3$ nanoparticles as indicated by BFI and SAED pattern in Fig. 7b and c, respectively.

Lattice image of a typical 50 nm-sized and twinned γ + δ $Al_2O_3$ particle taken after electron irradiation for 25 min (Fig. 8a) showed relaxed/recrystallized surface of the γ-type, with a relic γ + δ type core in [1 1 0] zone axis as indicated by 2-D forward and inverse Fourier transform in Fig. 8b and c, respectively. The 10 nm-sized γ-$Al_2O_3$ particles taken after 15 min of electron irradiation showed significant amorphization yet a relic {1 1 1}-faceted core of the γ-phase remained as indicated by 2-D forward transform in [1 1 0] zone axis (Fig. 9a). After 40 min of electron irradiation the nanoparticles were almost completely amorphized (Fig. 9b).

## 4. Discussion

### *4.1. Adsorption–desorption hysteresis loop characteristic of cylindrical mesopores*

Capillary condensation typically occurs for mesopores in a size range 2–50 nm to show type IV isotherm (Fig. A.1a), which can be classified into H1 to H4 subtypes (Fig. A.1b). According

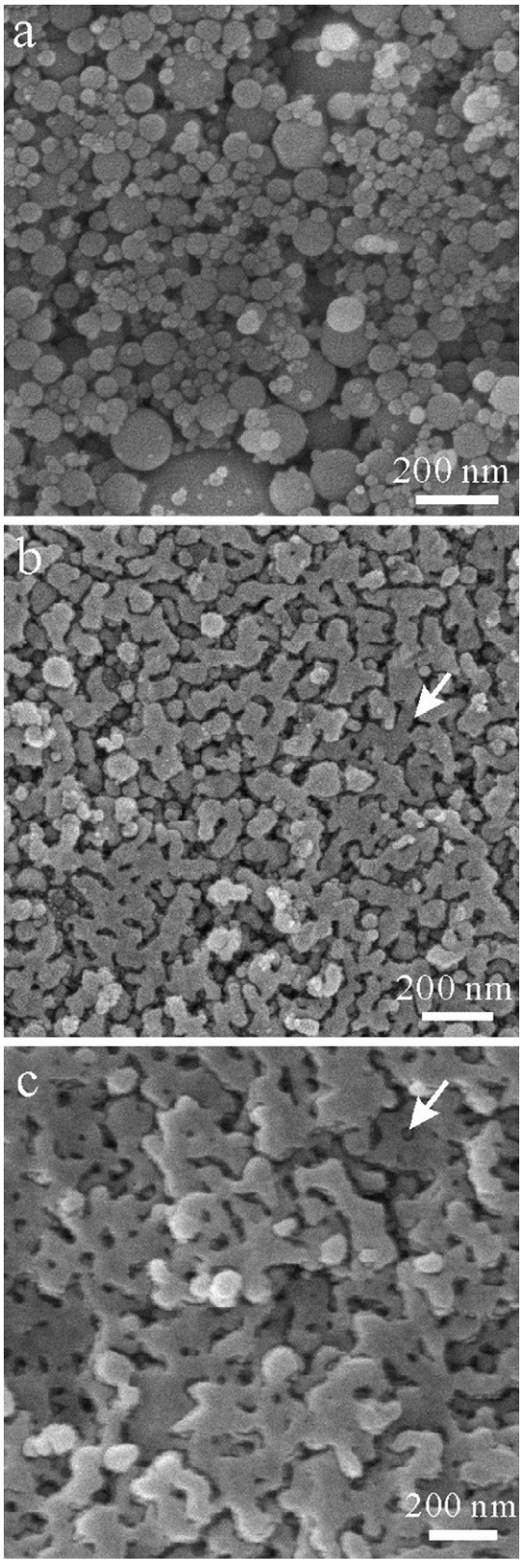


Fig. 5. SEM secondary electron image of the $Al_2O_3$ powder with an average diameter of 50 nm: (a) dry pressed and slightly agglomerated, (b) and (c) further heated at 1200 °C for 10 min and 1300 °C for 4 min to form cylindrical pores and truncated pores (arrow), respectively.

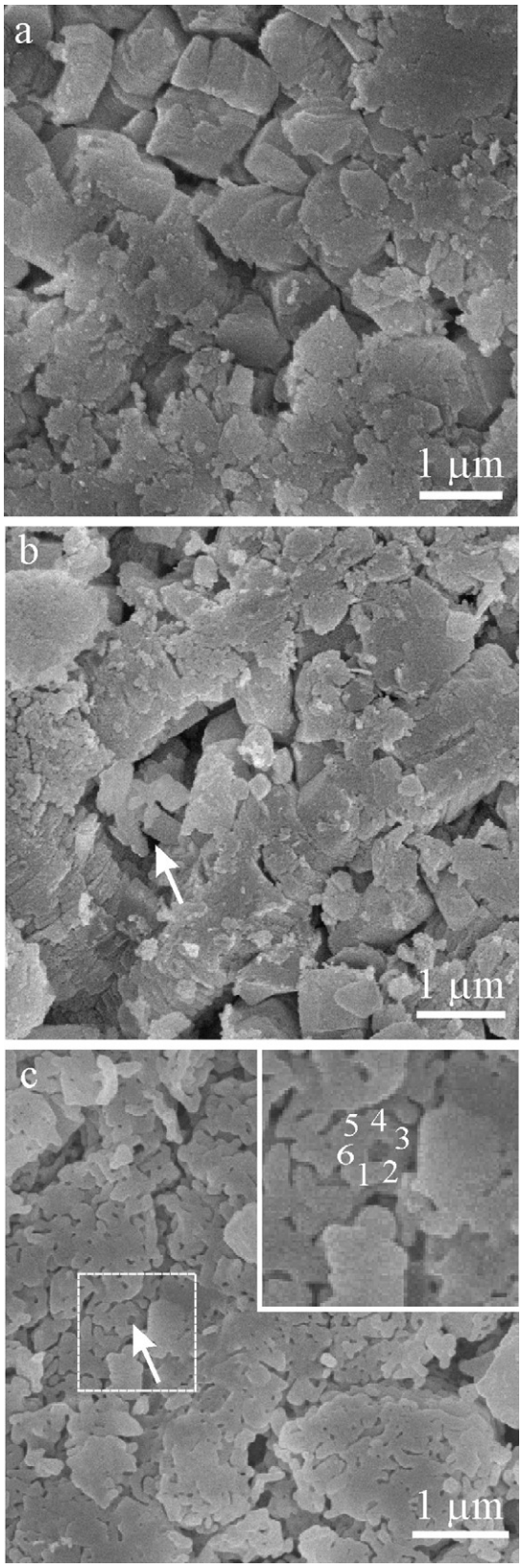


Fig. 6. SEM secondary electron image of the $Al_2O_3$ powder with an average diameter of 10 nm: (a) dry pressed and significantly agglomerated, (b) and (c) further heated at 1300 °C for 5 and 20 min to form cylindrical pores and truncated pores entrapped within the repacked nanoparticles (arrow), respectively. The arrowed region in (c) is magnified (inset) to show the individual particles (numbered) in coalescence (cf. text).

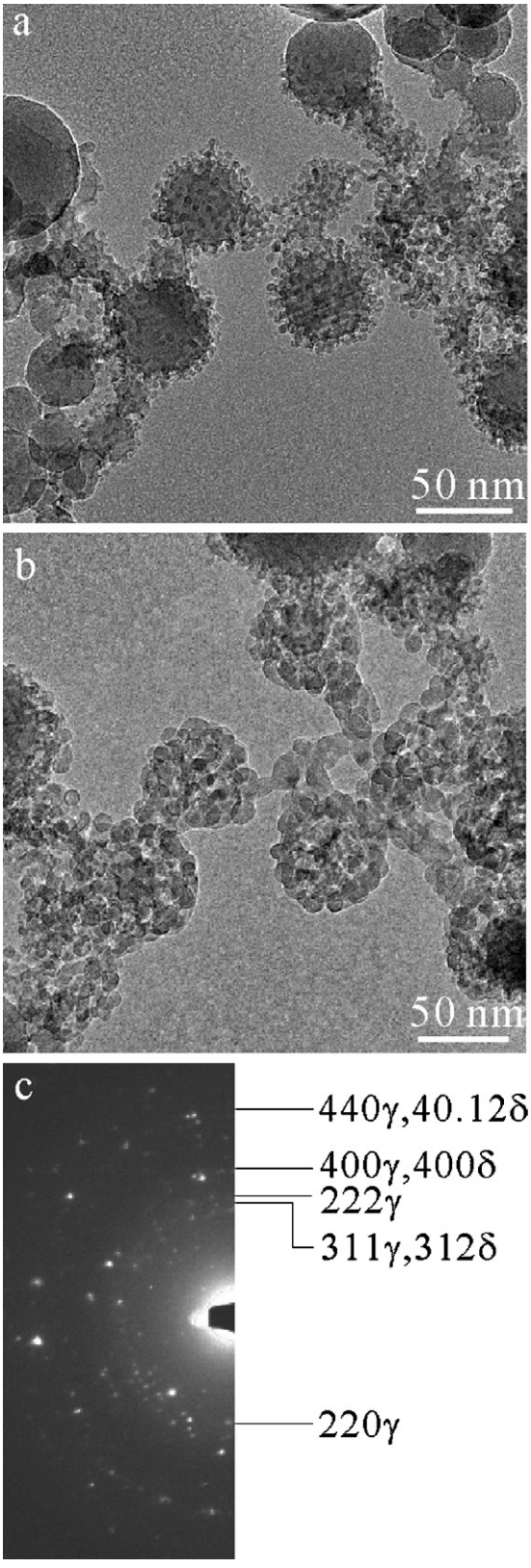


Fig. 7. TEM BFI of the $Al_2O_3$ powders with an average diameter of 50 nm taken (a) after electron irradiation for 30 min, showing the γ + δ-type particles underwent surface amorphization followed by cellular/dendritic crystallization to form new γ-$Al_2O_3$ droplets ca. 5 nm in diameter, (b) after electron irradiation for 60 min showing coarsening/repacking of newly formed γ-$Al_2O_3$ nanoparticles as indicated by SAED pattern in (c).

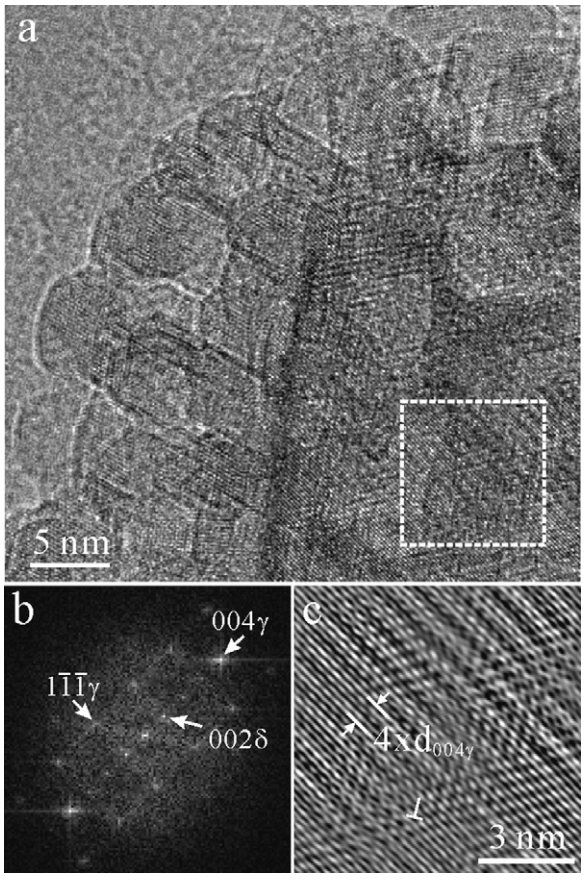


Fig. 8. (a) Lattice image of a typical 50 nm-sized and twinned γ + δ $Al_2O_3$ particle in [1 1 0] zone axis, the same as in Fig. 1c, taken after electron irradiation for 25 min, showing relaxed/recrystallized surface of the γ-type and a relic γ + δ core having dislocation (denoted as T) half plane parallel to (1 $\bar{1}$ $\bar{1}$)γ and (0 0 2)δ *d*-spacing 4 times that of (0 0 4)γ as indicated by 2-D (b) forward and (c) inverse Fourier transform of the square region in (a).

to the present observations of BJH $N_2$ adsorption–desorption isotherms, the dry pressed $Al_2O_3$ samples with γ-type related structures have a hysteresis loop somewhat between H1 and H2 type when prepared from 50 nm-sized powders, whereas a H4 type corresponding to narrow slit-like pores[21] when prepared from the 10 nm-sized powders having an average pore size (ca. 6 nm, Table 2) one third that of the former (ca. 20 nm, Table 1).

Regardless of the difference in powder size, those $Al_2O_3$ samples just went through an onset coarsening-coalescence event have cylindrical mesopores with a characteristic H1 type hysteresis loop similar to the case of other mesoporous materials with a pore width range 2–50 nm.[21] The kinetics to form cylindrical mesopores, however, depend on the size of the starting $Al_2O_3$ powders. Having a smaller pore size, the sample composed of 10 nm- rather than 50 nm-sized powders would promote pore migration and growth/coalescence at high temperatures. This accounts for a wider size distribution of pores and less well defined H1 type loop in a wider range of relative pressure for the 10 nm- than the 50 nm-sized powders upon firing. A longer firing time in the temperature range 1200–1400 °C improved but smeared the H1 type loop for the samples com-

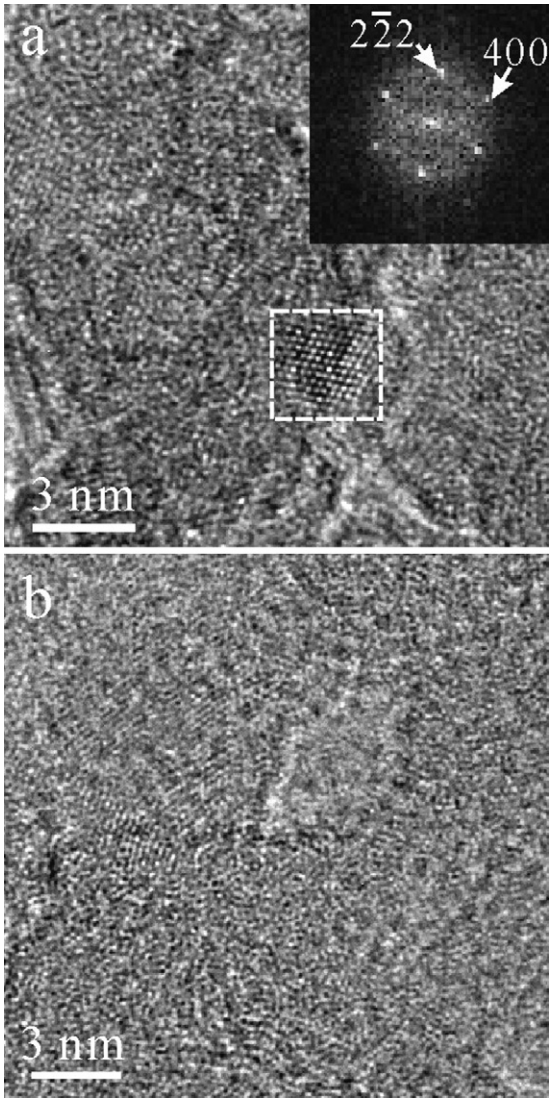


Fig. 9. (a) Lattice image of 10 nm-sized γ-$Al_2O_3$ particles taken after 15 min of electron irradiation showing significant amorphization yet still with a relic {1 1 1}-faceted core of the γ-phase in [1 1 0] zone axis as indicated by 2-D forward transform (inset) of the square region, (b) lattice image of the same sample taken after 40 min of electron irradiation showing nearly complete amorphization of the nanoparticles.

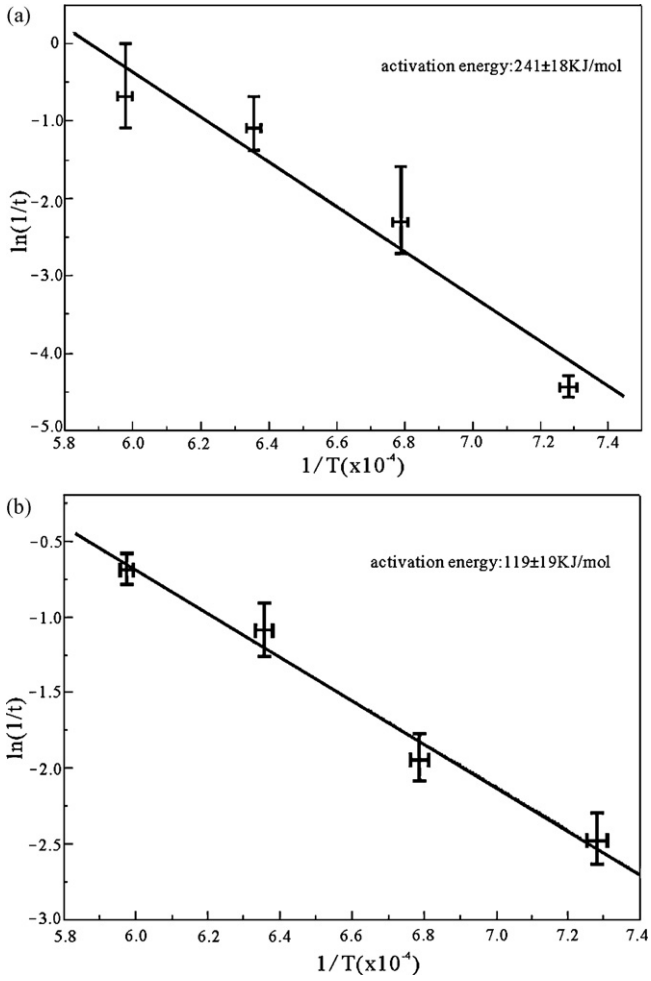


Fig. 10. Arrhenius plots of the logarithmic reciprocal time ($t_{0.5}$ and $t_{0.7}$ in min) against reciprocal temperature (in Kelvin) for the formation of cylindrical pores and specific surface area decrease by 50% and 70% from the dry pressed $Al_2O_3$ powders with an average particle size of (a) 50 nm and (b) 10 nm, respectively.

posed of 10 nm- and 50 nm-sized powders, respectively. This can be attributed to a more pronounced coarsening and repacking process of nanoparticles for effective sintering (cf. Fig. 7 of ref. [24]) and cylindrical pore formation, whereas necking of the cylindrical pores to form truncated pores for the sample composed of larger sized powders. Alternatively surface energy change due to size reduction and/or shape specification of the γ-type related $Al_2O_3$ particles may affect the kinetics of $N_2$ adsorption and desorption and hence the hysteresis loop.

### *4.2. Activation energy and diffusion mechanism for onset coarsening-coalescence*

On the basis of the appearance of the adsorption–desorption hysteresis loop characteristic of cylindrical mesopores (Fig. 3) and the drastic decrease of specific surface area by 50% (Table 1) in the linear region of the rate curves (Fig. A.4), the onset time $t_{0.5}$ for γ-type related $Al_2O_3$ powders 50 nm in diameter to coarsening and coalesce was determined as $85 \pm 10$, $10 \pm 5$, $3 \pm 1$ and $2 \pm 1$ min at 1100, 1200, 1300 and 1400 °C, respectively. The corresponding Arrhenius plot of the reciprocal time $t_{0.5}$ for onset coarsening-coalescence versus the reciprocal temperature in Kelvin gives an apparent activation energy $241 \pm 18$ kJ/mol considering the maximum uncertainty of each data point (Fig. 10a). As a comparison, the 10 nm-sized powders have a lower activation energy ($119 \pm 19$ kJ/mol) for onset coarsening-coalescence given the Arrhenius plot of the data points $12 \pm 2$, $7 \pm 1$, $3 \pm 0.5$ and $2 \pm 0.2$ min, i.e. $t_{0.7}$ for a more drastic decrease of specific surface area by 70% yet still in the linear region of the rate curves (Fig. A.5), at 1100, 1200, 1300 and 1400 °C, respectively in Fig. 10b.

The above activation energy for onset coarsening-coalescence of the 50 and 10 nm-sized $Al_2O_3$ particles with γ-type related structure concerns the surface diffusion of the particles to form cylindrical pores and has nothing to do with

the subsequent γ–δ–θ–α transformation. Further sintering of the α-type particles would involve surface diffusion[25] and then grain boundary diffusion with an activation energy as high as 328 kJ/mol.[6] A lower activation energy may imply a more excited surface state for the 10 nm-sized particles to coarsen-coalesce readily, although a sintering process could also be involved as indicated by a relative density ~0.85 for the 50 nm-sized sample heated at 1200 °C for 15 min. This argument is supported by a more significant shape change and amorphization of the 10 nm- than 50 nm-sized γ-$Al_2O_3$ particles upon electron irradiation with associated heating effect (Fig. 9). In this connection, density functional theory calculation of the energetically favorable (0 0 1) face of γ-$Al_2O_3$ has addressed several points.[26] In particular, when the face with tetrahedral aluminum is exposed in the bulk-terminated system, the surface reconstructs extensively, leading to exposure of the higher-density layer. When only a few layers are present, this reconstruction may even lead to the collapse of the system into a different structure.[25] The γ-$Al_2O_3$ nanoparticles may thus undergo extensive surface reconstruction into liquid like layer with 4- or 4.5-coordinated $Al^{3+}$ analogous to the case of stable or supercooled melt.[27–29] (The liquid alumina consists of predominantly 4-coordinated $Al^{3+}$ with an average Al coordination of 4.5 according to $^{27}Al$ magic-angle spinning NMR spectroscopy on liquid $Al_2O_3$.[28,29] Capillarity effect is presumably not high enough for coordination change into 6, which has been reported to occur significantly (>50%) at an applied pressure as high as 2.2 GPa for alkali-germanate melts.[30]) It is by no means clear, if there is an ordered liquid state near the specific surfaces of γ-$Al_2O_3$ analogous to the case of sapphire basal plane.[31]

### 4.3. Effect of specific surface area on the phase change of $Al_2O_3$

Specific surface area was known to affect the γ–α transformation of the individual $Al_2O_3$ particles. Having a lower surface energy than α-$Al_2O_3$ as mentioned,[10] γ-$Al_2O_3$ is favorable to have a specific area higher than 125 $m^2/g$.[32] On the other hand, the stable α-$Al_2O_3$ form is favored at larger size with a specific surface area typically lower than 50 $m^2/g$ at 800 °C.[10] The specific surface area of the γ-related structures, such as the δ- and θ-type involving tetragonal/orthorhombic and monoclinic distortion, respectively are expected to fall between that of the γ- and α-types. Having a rather high specific surface area (269 $m^2/g$, cf. Table 2) the dry pressed sample of 10 nm-sized powders indeed has predominant γ-type structure. However, the dry pressed sample with an average particle size of 50 nm remained as γ-, δ- and θ-phases despite a rather low specific surface area of 35 $m^2/g$ (Table 1). In fact, the transformation of γ-type to the stable α-$Al_2O_3$ involves oxygen framework change and requires annealing at temperatures as high as 1100 °C.[25,26] By contrast, polymorphic phase transitions between alumina structures based on fcc packing of oxygen, including γ, δ, and θ with increasing extent of distortion, involve cation ordering on the interstitial sites of the approximately undisturbed oxygen subcell,[1,33,34] and therefore could occur at lower temperatures or induced by an applied stress for martensitic transformations of the polymorphs with a slightly different density depending on the extent of lattice distortion.

Upon heating, the specific surface area significantly decreased in accompaniment with the γ–α transformation as indicated by the samples fired for more than 30 min at 1200 °C in particular the one made of larger sized (i.e. 50 nm) powders (Table 1.). This implies that the change of specific surface area in a slightly sintered body may trigger the γ–α transformation of $Al_2O_3$ at high temperatures.

### 4.4. Implications for the phase behavior of γ-$Al_2O_3$ in a dynamic process

Laser ablation condensation is an effective method of producing γ-$Al_2O_3$ nanoparticles more or less in agglomeration and coalescence due to the considerable associated heating effect.[15] The γ-$Al_2O_3$ nanocondensates tended to coalesce over well-developed {1 1 1} facets to form multiple twins or single crystal of larger size. The coalescence of the γ-$Al_2O_3$ condensates involves Brownian motion/rotation of the nanoparticles under the influence of radiant heating during pulsed laser ablation analogous to imperfect oriented attachment of $TiO_2$ rutile nanocondensates to form dislocations, faults and twins.[35] Radiant heating was suggested to be up to about 1000 °C[15] in view of the change of nano chain aggregates (NCA) into a close packed manner analogous to the case of $TiO_2$ condensates produced by gas evaporation method[16] or laser ablation condensation process.[17,18]

The present isothermal static heating results coupled with BET/BJH measurements further indicated that the γ-type related $Al_2O_3$ powders were able to coarsen-coalesce within minutes to an hour in the temperature range of 1100–1400 °C before transforming into α-type structure under the influence of surface area change. This supports our previous supposition that γ-type related $Al_2O_3$ NCA are able to coalesce and/or sinter into a close packed manner by radiant heating with a rather low activation energy via surface diffusion near 1000 °C in a dynamic laser ablation process. Such a rapid coalescence/sintering process may be extended to the phase behavior of γ-type derived δ as well as θ, θ′, θ″ (monoclinic) commonly encountered in alumina obtained by physical vapor deposition techniques,[1,33,34] and in natural dynamic settings such as the presolar stars.[36–38] Rapid coarsening-coalescence of ceramic nanoparticles in a dynamic or static heating process is also of engineering concern in view of the fact that conventionally brittle ceramics may become ductile permitting large plastic deformation at low temperature if the resultant polycrystal has crystal size limited to a few nanometers.[39] The ductility may simply originate from the diffusion flow of atoms along the intercrystalline interface of the sintered nanosize grains.

## 5. Conclusions

1. BET/BJH adsorption–desorption hysteresis isotherms of nanosized $Al_2O_3$ powders with γ-type related structures

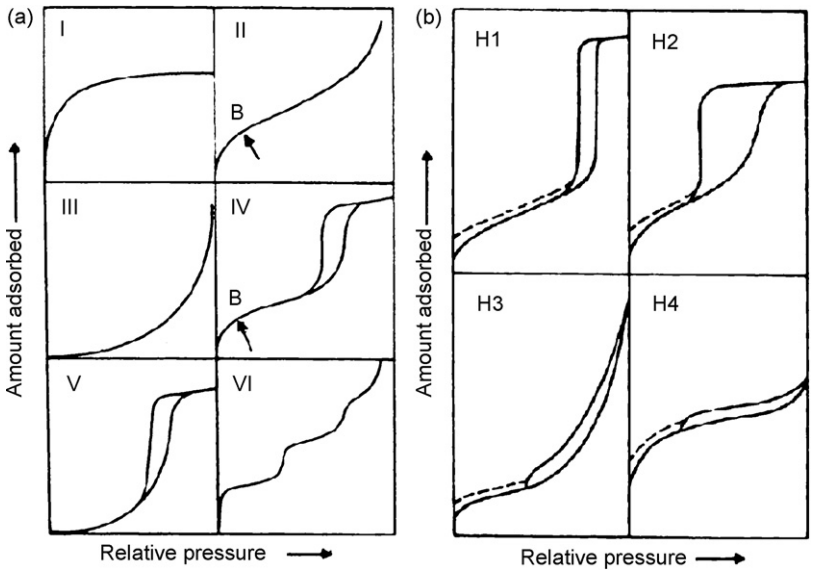


Fig. A.1. Types of (a) physisorption isotherms and (b) adsorption–desorption hysteresis loops after Sing et al. (1985)[21].

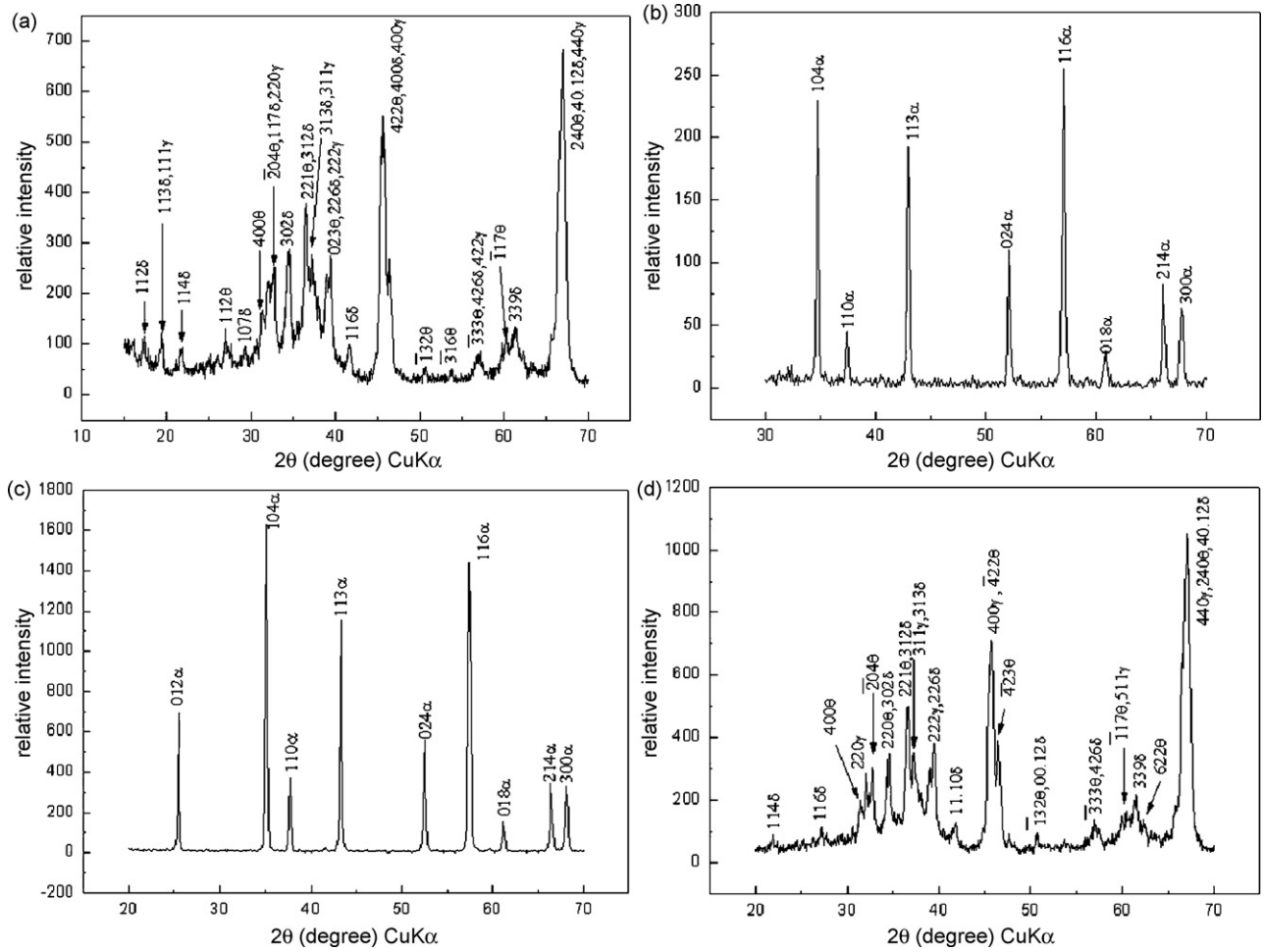


Fig. A.2. XRD (CuKα) traces of the $Al_2O_3$ powders with an average size of 50 nm subjected to various treatments: (a) dry pressing, (b), (c) and (d) further fired at 1200 °C for 30 min, 1300 °C for 30 min, and 1400 °C for 1 min, respectively having strong to moderate strong diffractions of the polymorphs labeled. The (*h k l*)s of γ, θ, and α phases are after JCPDS files 50-0741, 11-0517, and 46-1212, respectively, and those of δ phase are after Lippens and Boer (1964).[22]

were used satisfactorily to determine an incubation time for the formation of cylindrical pores and accompanied drastic change of specific surface area as a characteristic of an onset coarsening-coalescence event.

2. In the temperature range of 1100–1400 °C, the apparent activation energy for onset coarsening-coalescence of γ-type related $Al_2O_3$ nanoparticles before their transformation into α-type structure was determined as $241 \pm 18$ and $119 \pm 19$ kJ/mol, for 50 and 10 nm-sized powders, respectively indicating easier surface diffusion for the latter.
3. The size dependent surface state and onset coarsening-coalescence is supported by a rapid recrystallization–repacking process for the γ-type related $Al_2O_3$ nanoparticles upon electron beam heating.
4. The present static heating results of onset coarsening-coalescence of the γ-type related $Al_2O_3$ nanoparticles support our previous supposition that such particles in an assembly of nano chain aggregates are able to coalesce and/or sinter into a close packed manner by radiant heating near 1000 °C in a dynamic laser ablation process.

## Acknowledgments

We thank Drs. C.N. Pan, C.N. Huang and S.Y. Chen for helpful discussion on the coalescence of γ-type $Al_2O_3$ nanoparticles in a dynamic laser ablation condensation process and an anonymous referee for constructive comments. Supported by Center for Nanoscience and Nanotechnology at NSYSU and National Science Council, Taiwan, ROC under contract NSC95-2221-E-110-032-MY3.

## Appendix A

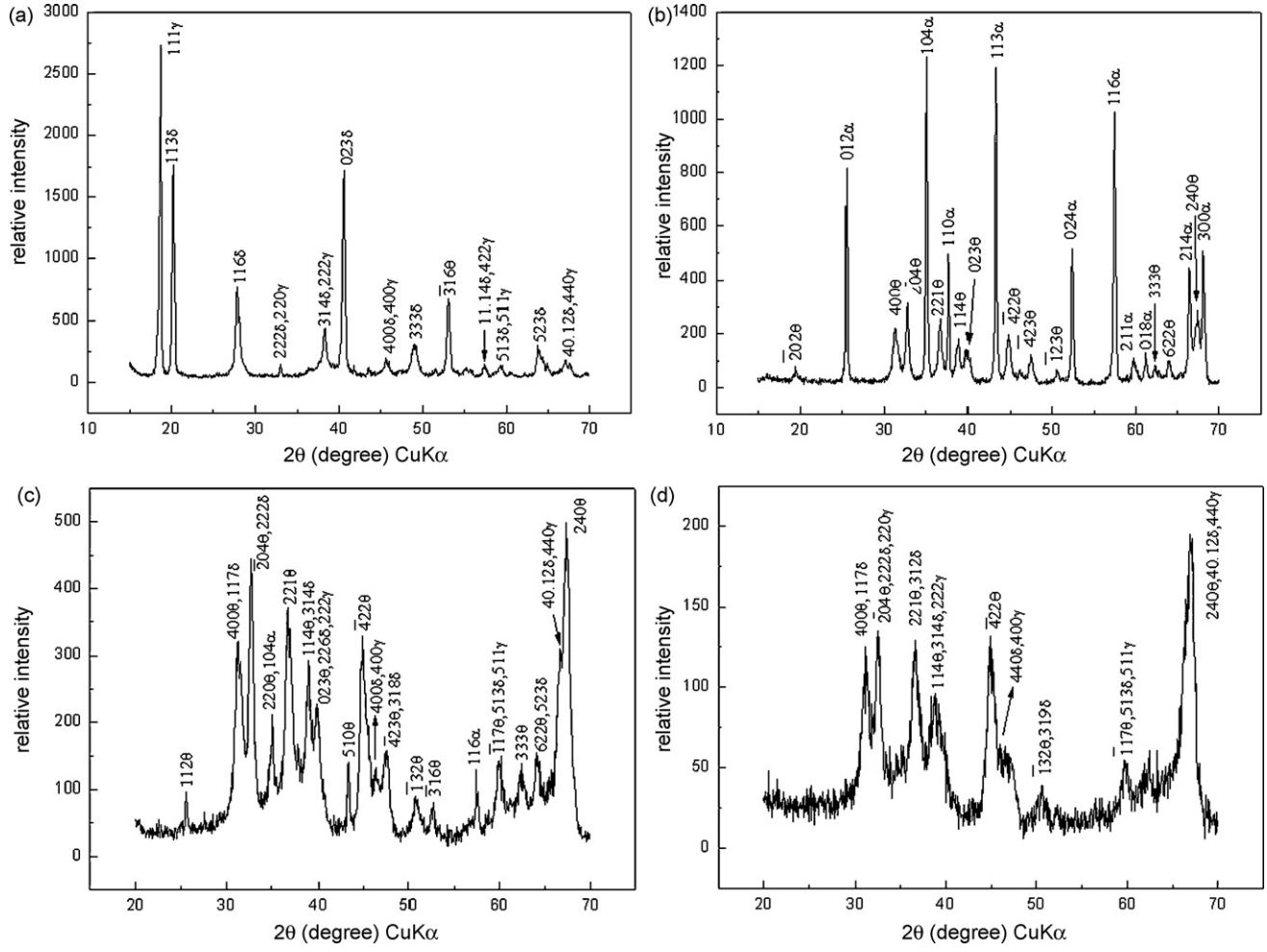


Fig. A.3. XRD (CuKα) traces of the $Al_2O_3$ powder with an average size of 10 nm subjected to various treatments: (a) dry pressing, (b), (c) and (d) further fired at 1200 °C for 30 min, 1300 °C for 5 min, and 1400 °C for 2 min, respectively having strong to moderate strong diffractions of the polymorphs labeled. The (*h k l*)s of γ, θ, and α phases are after JCPDS files 50-0741, 11-0517, and 46-1212, respectively, and those of δ phase are after Lippens and Boer (1964).[22] Note dry pressing of (1 1 1)-faceted γ + δ nanoparticles caused strong (1 1 1) preferred orientation in (a).

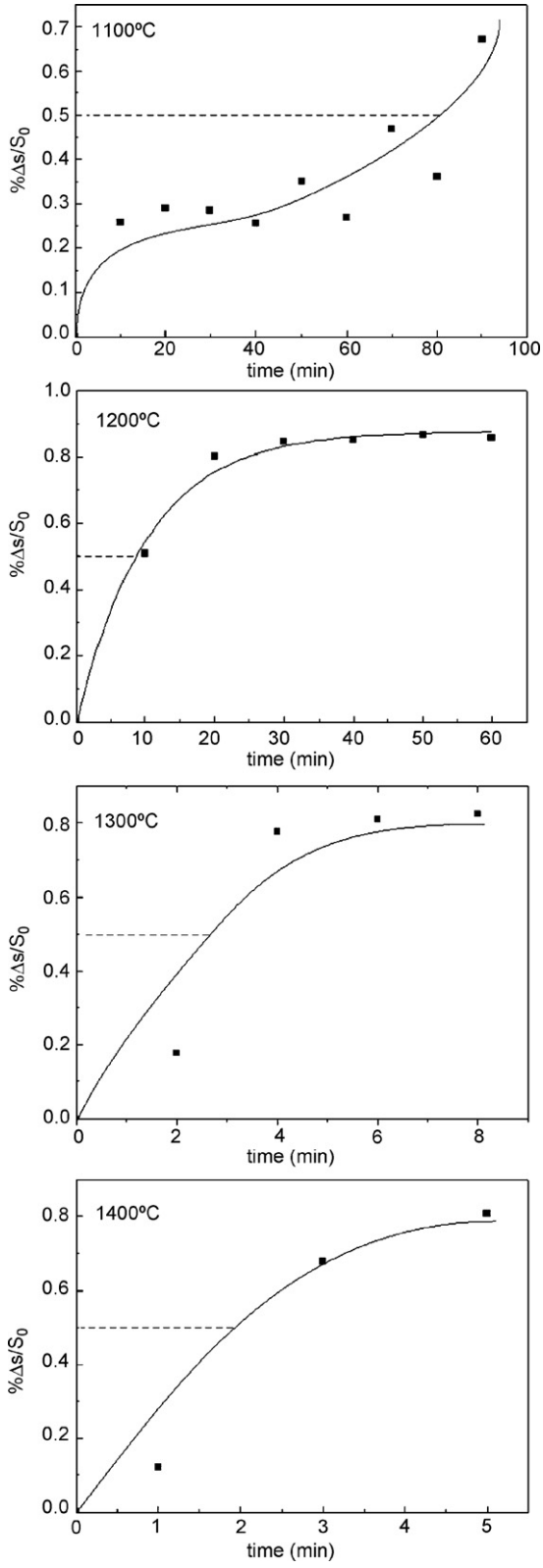


Fig. A.4. Observed rate curves in terms of per cent reduction of specific surface area ($\Delta S/S_o$, where $S_o$ is the initial quantity) versus time for 50-nm sized samples at specified temperatures. The time $t_{0.5}$, i.e. with 50% reduction of specific surface area as denoted by dashed line, used for activation energy estimation in Fig. 10 falls within an almost linear region. All rate curves, with the exception of that for 1100 °C, can be fitted to a general rate expression which will be analyzed in a later paper.

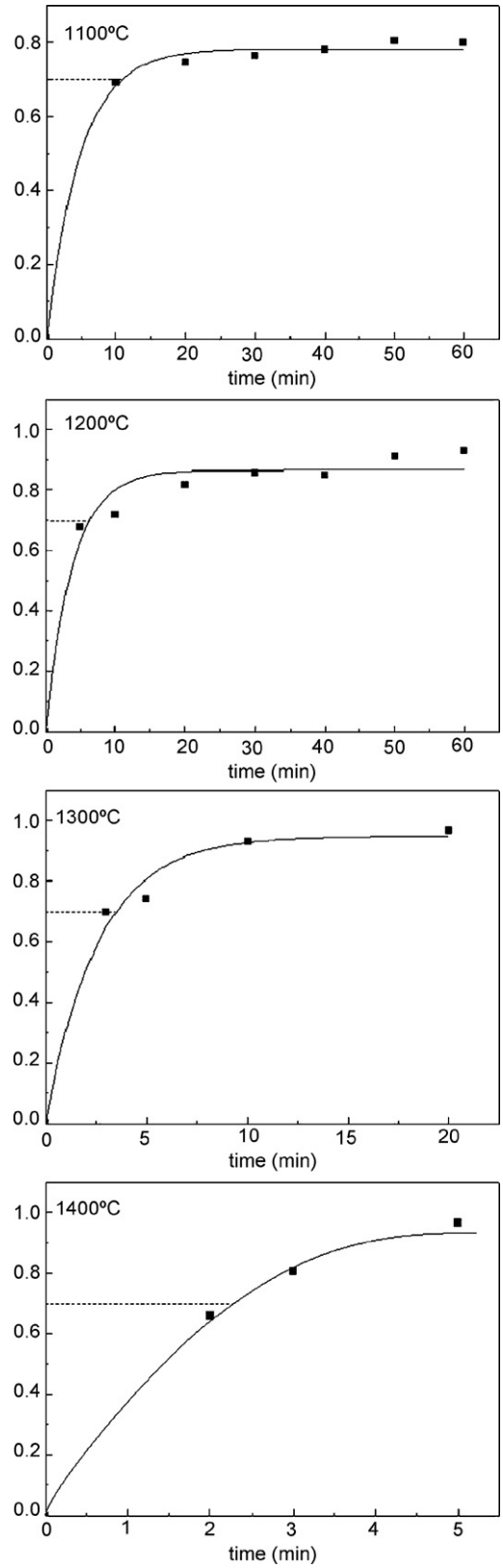


Fig. A.5. Observed rate curves in terms of per cent reduction of specific surface area versus time for 10-nm sized samples at specified temperatures. The time $t_{0.7}$, i.e. with 70% reduction of specific surface area as denoted by dashed line, used for activation energy estimation in Fig. 10 falls within an almost linear region. All rate curves can be fitted to a general rate law similar to that in Fig. A.4.

## References


1. Levin, I. and Brandon, D., Metastable alumina polymorphs: crystal structures and transition sequences. *J. Am. Ceram. Soc.*, 1998, **81**, 1995–2012.
2. Bennison, S. J. and Harmer, M. P., Microstructural studies of abnormal grain growth development in $Al_2O_3$. In *Ceramic Powders*, ed. P. Vincenzini. Elsevier, Amsterdam, 1983, pp. 929–938.
3. Goldstein, A. N., Echer, C. M. and Alivisatos, A. P., Melting in semiconductor nanocrystals. *Science*, 1992, **256**, 1425–1427.
4. Herring, C., Effect of change of scale on sintering phenomena. *J. Appl. Phys.*, 1950, **21**, 301–330.
5. Lim, L. C., Wong, P. M. and Jan, M., Microstructural evolution during sintering of near-monosized agglomerate-free submicron alumina powder compacts. *Acta Mater.*, 2000, **48**, 2263–2275.
6. Li, J. G. and Sun, X., Synthesis and sintering behavior of a nanocrystalline α-alumina powder. *Acta Mater.*, 2000, **48**, 3103–3112.
7. Karagedov, G. R. and Lyakhov, N. Z., Preparation and sintering of nanosize α-$Al_2O_3$ powder. *Nanostruct. Mater.*, 1999, **11**, 559–572.
8. Goodshaw, H. J., Forrester, J. S., Suaning, G. J. and Kisi, E. H., Sintering temperature depression in $Al_2O_3$ by mechanical milling. *J. Mater. Sci.*, 2007, **42**, 337–345.
9. McHale, J. M. and Navrotsky, A., Effect of increased surface area and chemisorbed $H_2O$ on the relative stability of nanocrystalline α-$Al_2O_3$ and γ-$Al_2O_3$. *J. Phys. Chem. B*, 1997, **101**, 603–613.
10. McHale, J. M., Auroux, A., Perrotta, A. J. and Navrotsky, A., Surface energies and thermodynamic phase stability in nanocrystalline aluminas. *Science*, 1997, **277**, 788–791.
11. Badkar, P. A. and Bailey, J. E., The mechanism of simultaneous sintering and phase transformation in alumina. *J. Mater. Sci.*, 1976, **11**, 1794–1806.
12. Ayral, A. and Phalippou, J., Submicrometer alumina powders. *Adv. Ceram. Mater.*, 1988, **3**, 575–579.
13. Tsai, D. S. and Hsieh, C. C., Controlled gelation and sintering of monolithic gels prepared from γ-alumina fume powder. *J. Am. Ceram. Soc.*, 1991, **74**, 830–836.
14. Tijburg, I. I. M., De Bruin, H., Elberse, P. A. and Geus, J. W., Sintering of pseudo-boehmite and γ-$Al_2O_3$. *J. Mater. Sci.*, 1991, **26**, 5945–5949.
15. Pan, C., Chen, S. Y. and Shen, P., Laser ablation condensation, coalescence and phase change of dense γ-$Al_2O_3$ particles. *J. Phys. Chem. B*, 2006, **110**, 24340–24345.
16. Jang, H. D. and Friedlander, S. K., Restructuring of chain aggregates of titania nanoparticles in the gas phase. *Aerosol Sci. Technol.*, 1998, **29**, 81–91.
17. Tsai, M. H., M.S. Thesis. National Sun Yat-sen University, Taiwan, 2002.
18. Tsai, M. H., Chen, S. Y. and Shen, P., Imperfect oriented attachment: accretion and defect generation of nanosize rutile condensates. *Nano Lett.*, 2004, **4**, 1197–1201.
19. Brunauer, S., Emmett, P. H. and Teller, E., Adsorption of gases in multimolecular layers. *J. Am. Chem. Soc.*, 1938, **60**, 309–319.
20. Barrett, E. P., Joyner, L. G. and Halenda, P. P., The determination of pore volume and area distribution in porous substances I. Computations from nitrogen isotherms. *J. Am. Chem. Soc.*, 1951, **73**, 373–380.
21. Sing, K. S. W., Everett, D. H., Haul, R. A. W., Moscou, L., Pierotti, R. A., Rouquerol, J. *et al.*, Reporting physisorption data for gas/solid systems with special reference to the determination of surface area and porosity. *Pure Appl. Chem.*, 1985, **57**, 603–619.
22. Lippens, B. C. and de Boer, J. H., Study of phase transformations during calcination of aluminum hydroxides by selected area electron diffraction. *Acta Cryst.*, 1964, **17**, 1312–1321.
23. Chang, P. L., Yen, F. S., Cheng, K. C. and Wen, H. L., Examinations on the critical and primary crystallite sizes during θ- to α-phase transformation of ultrafine alumina powders. *Nano Lett.*, 2001, **1**, 253–261.
24. Chen, P. L. and Chen, I. W., Sintering of fine oxide powders. *J. Am. Ceram. Soc.*, 1997, **80**, 637–645.
25. Teng, M. H., Marks, L. D. and Johnson, D. L., Computer simulations of interactions between ultrafine alumina particles produced by an arc discharge. *J. Mater. Res.*, 1997, **12**, 235–243.
26. Vijay, A., Mills, G. and Metiu, H., Structure of the (0 0 1) surface of γ alumina. *J. Chem. Phys.*, 2002, **117**, 4509–4516.
27. Ansell, S., Krishnan, S., Weber, J. K. R., Felten, J. J., Nordine, P. C., Beno, M. A. *et al.*, Structure of liquid aluminum oxide. *Phys. Rev. Lett.*, 1997, **78**, 464–466.
28. Coutures, J. P., Massiot, D., Bessada, C., Echegut, P., Rifflet, J. C. and Taulelle, F., A $^{27}$A1 NMR study of liquid aluminates in the 1600 °C–2100 °C temperature range. *C.R. Acad. Sci.*, 1990, **310**, 1041–1045.
29. Massiot, D., Taulelle, F. and Coutures, J. P., Structural diagnostic of high-temperature liquid-phases by Al-27 NMR. *J. Colloq. Phys. C.*, 1990, **51**, 5425–5431.
30. Farber, D. L. and Williams, Q., Pressure-induced coordination changes in alkali-germanate melts: an in situ spectroscopic investigation. *Science*, 1992, **256**, 1427–1430.
31. Oh, S. H., Kauffmann, Y., Scheu, C., Kaplan, W. D. and Rühle, M., Ordered liquid aluminum at the interface with sapphire. *Science*, 2005, **310**, 661–663.
32. Lowell, S. and Shields, J. E., *Powder Surface Area and Porosity*. Chapman and Hall, London, U.K, 1984, pp. 3–5, 17–29.
33. Levin, I. and Brandon, D., A new alumina polymorph with monoclinic symmetry. *Philos. Mag. Lett.*, 1998, **77**, 117–124.
34. Chou, T. C. and Nieh, T. G., Nucleation and concurrent anomalous grain growth. *J. Am. Ceram. Soc.*, 1991, **74**, 2270–2279.
35. Tsai, M. H., Shen, P. and Chen, S. Y., Defects generation of anatase nanocondensates via coalescence and transformation from dense fluorite-type $TiO_2$. *J. Appl. Phys.*, 2006, **100**, 114313-1–114313-6.
36. Choi, B. G., Huss, G. R., Wasserburg, G. J. and Galline, R., Presolar corundum and spinel in ordinary chondrites: origins from AGB stars and a supernova. *Science*, 1998, **2282**, 1284–1289.
37. Ash, R., Origin and early evolution of solid matter in the solar system. *Meteorities Planetary Sci.*, 2001, **36**, 583–584.
38. Stroud, R. M., Nittler, L. R. and O'D Alexander, C. M., Polymorphism in presolar $Al_2O_3$ grains from asymptotic giant branch stars. *Science*, 2004, **305**, 1455–1457.
39. Karch, J., Birringer, R. and Gleiter, H., Ceramics ductile at low temperature. *Nature*, 1987, **330**, 556–558.